

Pb₂TiOF(SeO₃)₂Cl and Pb₂NbO₂(SeO₃)₂Cl: Small Changes in Structure Induced A Very Large SHG Enhancement

Xue-Li Cao, Chun-Li Hu, Xiang Xu, Fang Kong and Jiang-Gao Mao*

Electronic Summplementary Information

1. Syntheses of Pb₂TiOF(SeO₃)₂Cl and Pb₂NbO₂(SeO₃)₂Cl.

2. Instrumentations for physical property measurements.

3. Computational Descriptions.

4. Tables and Figures

Table S1. Crystal data and structural refinements for the two compounds.

Table S2. Selected bond distances (Å) for the two compounds.

Table S3. The state energies (eV) of the lowest conduction band (L-CB) and the highest valence band (H-VB) of Pb₂TiOF(SeO₃)₂Cl and Pb₂NbO₂(SeO₃)₂Cl.

Table S4. The experimental and calculated optical data for two compounds. From top to bottom the data are, in order, the experimental and calculated band gaps, the static SHG coefficients, the powder SHG effects, the calculated dipole moment.

Table S5. The re-evaluated SHG coefficients with different band gaps. The bold values on the diagonal are the original ones.

Table S6. The re-evaluated SHG coefficients by replacing the band structure (E) or momentum matrix elements (M) of one compound with the other compound's. For example, the value corresponding to E(Pb-Ti-O-F) and M(Pb-Nb-O) means using the band structure from Pb₂TiOF(SeO₃)₂Cl and using the momentum matrix element from

$\text{Pb}_2\text{NbO}_2(\text{SeO}_3)_2\text{Cl}$. The bold values on the diagonal are the original ones.

Figure S1. Simulated and experimental XRD powder patterns of $\text{Pb}_2\text{TiOF}(\text{SeO}_3)_2\text{Cl}$ (a) and $\text{Pb}_2\text{NbO}_2(\text{SeO}_3)_2\text{Cl}$ (b).

Figure S2. The coordination geometries around the Ti and Pb atoms in $\text{Pb}_2\text{TiOF}(\text{SeO}_3)_2\text{Cl}$.

Figure S3. The coordination environments around the Nb atom (a), Pb(1) atom (b) and Pb(2) atom (c) in $\text{Pb}_2\text{NbO}_2(\text{SeO}_3)_2\text{Cl}$.

Figure S4. Thermogravimetric analysis (TGA) and Differential scanning calorimetry (DSC) curves of $\text{Pb}_2\text{TiOF}(\text{SeO}_3)_2\text{Cl}$ (a), and $\text{Pb}_2\text{NbO}_2(\text{SeO}_3)_2\text{Cl}$ (b).

Figure S5. IR spectra of $\text{Pb}_2\text{TiOF}(\text{SeO}_3)_2\text{Cl}$ (a) and $\text{Pb}_2\text{NbO}_2(\text{SeO}_3)_2\text{Cl}$ (b).

Figure S6. UV-Vis absorption spectra of $\text{Pb}_2\text{TiOF}(\text{SeO}_3)_2\text{Cl}$ (a) and $\text{Pb}_2\text{NbO}_2(\text{SeO}_3)_2\text{Cl}$ (b).

Figure S7. Oscilloscope traces of the SHG signals for the powders (149-210 μm) of KTP, $\text{Pb}_2\text{TiOF}(\text{SeO}_3)_2\text{Cl}$ and $\text{Pb}_2\text{NbO}_2(\text{SeO}_3)_2\text{Cl}$ (a), and phase-matching curve for $\text{Pb}_2\text{TiOF}(\text{SeO}_3)_2\text{Cl}$ and $\text{Pb}_2\text{NbO}_2(\text{SeO}_3)_2\text{Cl}$ (b) on a 2.05 μm Q-switched Nd:YAG laser. The curve drawn is to guide the eye and not a fit to the data.

Figure S8. Polarization versus applied electric field for $\text{Pb}_2\text{TiOF}(\text{SeO}_3)_2\text{Cl}$ (a) and $\text{Pb}_2\text{NbO}_2(\text{SeO}_3)_2\text{Cl}$ (b).

Figure S9. The scissor-added band structures of $\text{Pb}_2\text{TiOF}(\text{SeO}_3)_2\text{Cl}$ (a), and $\text{Pb}_2\text{NbO}_2(\text{SeO}_3)_2\text{Cl}$ (b).

Figure S10. The partial density of states (PDOS) of $\text{Pb}_2\text{TiOF}(\text{SeO}_3)_2\text{Cl}$ (a-b) and $\text{Pb}_2\text{NbO}_2(\text{SeO}_3)_2\text{Cl}$ (c-d).

Figure S11. The highest occupied molecular orbital (HOMO) and the lowest unoccupied molecular orbital (LUMO) of $\text{Pb}_2\text{TiOF}(\text{SeO}_3)_2\text{Cl}$ (a: HOMO, b: LUMO) and $\text{Pb}_2\text{NbO}_2(\text{SeO}_3)_2\text{Cl}$ (c: HOMO, d: LUMO).

1. Syntheses of $\text{Pb}_2\text{TiOF}(\text{SeO}_3)_2\text{Cl}$ and $\text{Pb}_2\text{NbO}_2(\text{SeO}_3)_2\text{Cl}$.

Materials: PbCl_2 (99+%, AR), TiO_2 (98+%, AR), Nb_2O_5 (99+%, AR), SeO_2 (99+%, AR), and hydrofluoric acid were used as received. All of the chemicals were supplied by the Shanghai Reagent Factory.

Syntheses: $\text{Pb}_2\text{TiOF}(\text{SeO}_3)_2\text{Cl}$ and $\text{Pb}_2\text{NbO}_2(\text{SeO}_3)_2\text{Cl}$ were prepared by using hydrothermal techniques. The loaded compositions are PbCl_2 (166.9 mg, 0.6 mmol), TiO_2 (63.9 mg, 0.8 mmol), SeO_2 (111.0 mg, 1.0 mmol), HF (0.10 mL) and H_2O (6 mL) for $\text{Pb}_2\text{TiOF}(\text{SeO}_3)_2\text{Cl}$, and PbCl_2 (139.1 mg, 0.5 mmol), Nb_2O_5 (53.2 mg, 0.4 mmol), and SeO_2 (221.9 mg, 2 mmol), HF (0.10mL) and H_2O (6mL) for $\text{Pb}_2\text{NbO}_2(\text{SeO}_3)_2\text{Cl}$. The reactions were carried out at 230 °C for 6 days for $\text{Pb}_2\text{TiOF}(\text{SeO}_3)_2\text{Cl}$ and 210 °C for 4 days for $\text{Pb}_2\text{NbO}_2(\text{SeO}_3)_2\text{Cl}$. The final pH values of the reaction media are both close to 0.5. Rod-shaped crystals of $\text{Pb}_2\text{TiOF}(\text{SeO}_3)_2\text{Cl}$ were obtained in a yield of about 46% based on Pb along with small amount of single crystals of PbClF and $\text{Pb}_3(\text{SeO}_3)_2\text{Cl}_2$ as impurities which were removed manually based on their different shapes. Colorless rod-shaped crystals of $\text{Pb}_2\text{NbO}_2(\text{SeO}_3)_2\text{Cl}$ were recovered as single phase in a yield of about 78% based on Pb after the removal of the impurity $\text{Pb}_3(\text{SeO}_3)_2\text{Cl}_2$ crystals through manually picking.

2. Instrumentations for physical property measurements.

All of the chemicals were purchased from commercial sources and used without further purification. Data collections for $\text{Pb}_2\text{TiOF}(\text{SeO}_3)_2\text{Cl}$ and $\text{Pb}_2\text{NbO}_2(\text{SeO}_3)_2\text{Cl}$ were performed on a SuperNova, Dual, Cu at zero, Atlas equipped with a graphite-monochromated Mo-K α radiation ($\lambda = 0.71073 \text{ \AA}$) at 293(2) K. Both structures were solved by the direct methods and refined anisotropically by using SHELXTL-97.^[1] Microprobe elemental analyses were performed on a field emission scanning electron microscope (FESEM, JSM6700F) equipped with an energy dispersive X-ray spectroscope (EDS, Oxford INCA). The X-ray powder diffraction data were collected on a Panalytical X'pert Pro MPD diffractometer using graphite-monochromated Cu-K α radiation in the 2θ range of 5-60° with a step size of 0.02°. TGA and DTA studies were all carried out with a NETZSCH STA 449C instrument. The sample and reference (Al_2O_3) were enclosed in a platinum crucible and heated at a rate of 10 °C/min from room temperature to 1000 °C under a nitrogen atmosphere. The IR spectra were recorded on a Magna 750 FT-IR spectrometer as KBr pellets in the range of 4000–400 cm^{-1} . The UV absorption and Optical diffuse reflectance spectra were measured at room temperature with a PE Lambda 900 UV-Visible spectrophotometer in the range of 190-2500 nm. BaSO_4 plate was used as a standard (100 % reflectance). The absorption spectra were calculated from reflectance spectrum using the Kubelka-Munk function:^[2] $\alpha/S = (1-R)^2/2R$, where α is the absorption coefficient, S is the scattering coefficient which is practically wavelength independent when the particle size is larger than 5 μm , and R is the reflectance. The measurements of the powder frequency-doubling effect were carried out by means of the method of Kurtz and Perry.^[3] The fundamental wavelength is 1064 nm generated by a Q-switched Nd:YAG laser. The SHG wavelength is 532 nm. KH_2PO_4 (KDP) was used as reference to assume the effect. SHG efficiency has been shown to depend strongly on particle size, thus samples of KDP,

and $\text{Pb}_2\text{TiOF}(\text{SeO}_3)_2\text{Cl}$ and $\text{Pb}_2\text{NbO}_2(\text{SeO}_3)_2\text{Cl}$ were ground and sieved into several distinct particle size ranges (25-44, 44-53, 53-74, 74-105, 105-149, 149-210, 210-300 μm). All of the samples were placed in separate capillary tubes. No index-matching fluid was used in any of the experiments. SHG measurements were also performed on a 2.05 μm Q-switch laser and KTP (KTiOPO_4) was used as reference. The ferroelectric properties of the two compounds were measured on an aixACCT TF Analyzer 2000E ferroelectric tester at room temperature. $\text{Pb}_2\text{TiOF}(\text{SeO}_3)_2\text{Cl}$ powder was pressed into a pellet (6-mm-diameter and 0.5-mm-thick) whereas $\text{Pb}_2\text{NbO}_2(\text{SeO}_3)_2\text{Cl}$ powder was pressed into a pellet (9.8-mm-diameter and 0.94-mm-thick), and the conducting Ag-glue was applied on the both sides of the pellet surfaces for electrodes.

3. Computational Descriptions.

All calculations were carried out by using the total-energy code of CASTEP.^[4] The total energy was calculated within the framework of nonlocal gradient-corrected approximations [Perdew-Burke-Ernzerhof (PBE) functional].^[5] The interactions between the ionic cores and the electrons was described by the norm-conserving pseudopotential.^[6] The following orbital electrons were treated as valence electrons: Pb-5d¹⁰6s²6p², Nb-4d⁴5s¹, Ti-3d²4s², Se-4s²4p⁴, O-2s²2p⁴, F-2s²2p⁵, and Cl-3s²3p⁵. The numbers of plane waves included in the basis sets were determined by a cutoff energy of 850 and 820 eV for Pb₂TiOF(SeO₃)₂Cl and Pb₂NbO₂(SeO₃)₂Cl, respectively. The numerical integration of the Brillouin zone was performed using a Monkhorst-Pack *k*-point sampling of 3 × 5 × 3. The other parameters and convergent criteria were the default values of CASTEP code.

The calculation of second-order NLO properties were based on length-gauge formalism within the independent-particle approximation.^[7] We adopted the Chen's static formula, which has been derived by Rashkeev et al.^[8] and later improved by Chen's group.^[9] The static second-order NLO susceptibility can be expressed as

$$\chi^{\alpha\beta\gamma} = \chi^{\alpha\beta\gamma}(VE) + \chi^{\alpha\beta\gamma}(VH) + \chi^{\alpha\beta\gamma}(\text{two bands})$$

where $\chi^{\alpha\beta\gamma}(VE)$ and $\chi^{\alpha\beta\gamma}(VH)$ give the contributions to $\chi^{\alpha\beta\gamma}$ from virtual-electron processes and virtual-hole processes, respectively; $\chi^{\alpha\beta\gamma}(\text{two bands})$ is the contribution to $\chi^{\alpha\beta\gamma}$ from the two-band processes. The formulas for calculating $\chi^{\alpha\beta\gamma}(VE)$, $\chi^{\alpha\beta\gamma}(VH)$, and $\chi^{\alpha\beta\gamma}(\text{two bands})$ are given in Ref. 9 It's worth noting that more than 300 empty bands were involved in the calculations to ensure the convergence of SHG coefficients. In addition, DFT-GGA usually underestimates the conduction bands energies, so the conduction bands energy

should be shifted upward by adding a scissor operator to agree with measured values of the band gap.^[7-8]

References:

- [1] G. M. Sheldrick, SHELXTL, *Crystallographic Software Package*, Version 5.1, Bruker-AXS: Madison, WI, 1998.
- [2] P. Kubelka, F. Z. Munk, *Tech. Phys.* 1931, **12**, 593.
- [3] S. W. Kurtz, T. T. Perry, *J. Appl. Phys.* 1968, **39**, 3798.
- [4] a) M. D. Segall, P. L. D. Lindan, M. J. Probert, C. J. Pickard, P. J. Hasnip, S. J. Clark, and M. C. Payne, *J. Phys.: Cond. Matt.* 2002, **14**, 2717. b) V. Milman, B. Winkler, J. A. White, C. J. Pickard, M. C. Payne, E. V. Akhmatkaya, and R. H. Nobes, *Int. J. Quantum Chem.* 2000, **77**, 895.
- [5] J. P. Perdew, K. Burke, and M. Ernzerhof, *Phys. Rev. Lett.* 1996, **77**, 3865.
- [6] J. S. Lin, A. Qteish, M. C. Payne, and V. Heine, *Phys. Rev.* 1993, **B 47**, 4174.
- [7] Aversa, C.; Sipe, J. E. *Phys. Rev. B* 1995, **52**, 14636.
- [8] Rashkeev, S. N.; Lambrecht, W. R. L.; Segall, B. *Phys. Rev. B* 1998, **57**, 3905.
- [9] Lin, J.; Lee, M. H.; Liu, Z. P.; Chen, C. T.; Pickard, C. J. *Phys. Rev. B* 1999, **60**, 13380.

4. Tables and Figures

Table S1. Crystal data and structural refinements for the two compounds.

Formula	Pb ₂ TiOF(SeO ₃) ₂ Cl	Pb ₂ NbO ₂ (SeO ₃) ₂ Cl
fw	786.65	828.66
crystal system	monoclinic	monoclinic
space group	<i>P2</i> ₁	<i>P2</i> ₁
<i>a</i> /Å	8.2863(5)	8.5110(5)
<i>b</i> /Å	5.3781(2)	5.4148(2)
<i>c</i> /Å	10.7167(6)	10.7300(6)
α (deg)	90	90
β (deg)	111.191(6)	111.753(7)
γ (deg)	90	90
<i>V</i> /Å ³	445.29(4)	459.28(4)
<i>Z</i>	2	2
<i>D</i> _c (g·cm ⁻³)	5.867	5.992
μ (Mo-K α) (mm ⁻¹)	47.087	46.023
GOF on F ²	1.055	1.062
Flack factor	0.0134(6)	0.0071(4)
R1, wR2 (I > 2 σ (I)) ^a	0.0330, 0.0750	0.0313, 0.0680
R1, wR2 (all data)	0.0342, 0.0756	0.0333, 0.0686

$$^a R1 = \sum ||F_o| - |F_c|| / \sum |F_o|, wR2 = \{ \sum w[(F_o)^2 - (F_c)^2]^2 / \sum w[(F_o)^2]^2 \}^{1/2}.$$

Table S2. Selected bond distances (Å) for the two compounds.

Pb ₂ TiOF(SeO ₃) ₂ Cl					
Pb(1)-O(3)	2.545(10)	Pb(2)-O(4)	2.591(10)	Ti(1)-O(1)#6	2.054(9)
Pb(1)-O(5)#1	2.652(12)	Pb(2)-O(5)#1	2.730(11)	Ti(1)-O(2)#2	2.145(10)
Pb(1)-O(6)	2.661(11)	Pb(2)-O(5)#3	2.764(11)	Se(1)-O(3)	1.683(9)
Pb(1)-O(2)#1	2.688(10)	Pb(2)-F(1)#4	2.818(8)	Se(1)-O(2)	1.707(10)
Pb(1)-O(4)	2.692(12)	Pb(2)-Cl(1)#5	2.895(4)	Se(1)-O(1)	1.722(10)
Pb(1)-O(1)	2.905(10)	Pb(2)-Cl(1)#3	3.082(4)	Se(2)-O(5)	1.683(12)
Pb(1)-Cl(1)	3.000(4)	Ti(1)-O(7)	1.770(9)	Se(2)-O(4)	1.705(11)
Pb(1)-O(1)#2	3.082(10)	Ti(1)-F(1)	1.889(8)	Se(2)-O(6)	1.711(10)
Pb(2)-O(3)#3	2.520(9)	Ti(1)-O(7)#4	1.915(9)		
Pb(2)-O(4)#3	2.556(12)	Ti(1)-O(6)	1.984(10)		
Pb ₂ NbO ₂ (SeO ₃) ₂ Cl					
Pb(1)-O(3)	2.524(9)	Pb(2)-O(3)#3	2.636(9)	Nb(1)-O(2)#2	2.127(9)
Pb(1)-O(4)	2.577(10)	Pb(2)-O(8)#4	2.642(9)	Nb(1)-O(6)	2.204(8)
Pb(1)-O(5)#1	2.584(10)	Pb(2)-O(5)#1	2.679(11)	Se(1)-O(3)	1.668(8)
Pb(1)-O(6)	2.634(9)	Pb(2)-O(5)#3	2.816(11)	Se(1)-O(2)	1.717(9)
Pb(1)-O(2)#1	2.846(10)	Pb(2)-Cl(1)#5	2.914(4)	Se(1)-O(1)	1.746(10)
Pb(1)-Cl(1)	2.934(3)	Pb(2)-Cl(1)#3	3.140(4)	Se(2)-O(5)	1.697(10)
Pb(1)-O(1)	3.123(10)	Nb(1)-O(8)	1.771(9)	Se(2)-O(6)	1.698(9)
Pb(1)-O(1)#2	3.182(10)	Nb(1)-O(7)	1.905(9)	Se(2)-O(4)	1.713(10)
Pb(2)-O(4)	2.526(9)	Nb(1)-O(7)#4	1.944(9)		
Pb(2)-O(4)#3	2.615(10)	Nb(1)-O(1)#6	2.097(9)		

Symmetry transformations used to generate equivalent atoms:

For Pb₂TiOF(SeO₃)₂Cl: #1 x, y+1, z; #2 -x+2, y+1/2, -z+2; #3 -x+1, y+1/2, -z+1; #4 -x+1, y+1/2, -z+2; #5 -x+1, y-1/2, -z+1; #6 -x+2, y-1/2, -z+2;

For Pb₂NbO₂(SeO₃)₂Cl: #1 x, y-1, z; #2 -x, y-1/2, -z; #3 -x+1, y-1/2, -z+1; #4 -x+1, y-1/2, -z; #5 -x+1, y+1/2, -z+1; #6 -x, y+1/2, -z;

Table S3. The state energies (eV) of the lowest conduction band (L-CB) and the highest valence band (H-VB) of the two compounds

Compound	k-point	L-CB	H-VB
Pb ₂ TiOF(SeO ₃) ₂ Cl	Z (0.000, 0.000, 0.500)	2.87376	0
	G (0.000, 0.000, 0.000)	2.85246	-0.11017
	Y (0.000, 0.500, 0.000)	3.26176	-0.05987
	A (-0.500, 0.500, 0.000)	3.27061	-0.28939
	B (-0.500, 0.000, 0.000)	2.87987	-0.18944
	D (-0.500, 0.000, 0.500)	2.87082	-0.22797
	E (-0.500, 0.500, 0.500)	3.28821	-0.34086
	C (0.000, 0.500, 0.500)	3.26434	-0.04913
Pb ₂ NbO ₂ (SeO ₃) ₂ Cl	Z (0.000, 0.000, 0.500)	2.37604	0
	G (0.000, 0.000, 0.000)	2.35862	-0.12251
	Y (0.000, 0.500, 0.000)	3.48962	-0.06538
	A (-0.500, 0.500, 0.000)	3.49315	-0.25536
	B (-0.500, 0.000, 0.000)	2.38872	-0.138
	D (-0.500, 0.000, 0.500)	2.39632	-0.15445
	E (-0.500, 0.500, 0.500)	3.53025	-0.20261
	C (0.000, 0.500, 0.500)	3.45676	-0.01432

Table S4. The experimental and calculated optical data for the two compounds. From top to bottom the data are, in order, the experimental and calculated band gaps, the static SHG coefficients, the powder SHG effects, the calculated dipole moment.

		Pb ₂ TiOF(SeO ₃) ₂ Cl	Pb ₂ NbO ₂ (SeO ₃) ₂ Cl
E_g (eV)	exp.	3.34	3.67
	cal.	2.82	2.28
	scissor	0.52	1.39
The absolute value of SHG coefficients ($\times 10^{-9}$ esu)		$d_{14}= 5.04$ $d_{16}= 3.65$ $d_{22}= 13.12$ $d_{23}= 0.93$	$d_{14}= 0.67$ $d_{16}= 0.38$ $d_{22}= 4.31$ $d_{23}= 2.42$
Exp. SHG effects (\times KDP)		9.6	2.3
Dipole moment (D/unit cell)		23.8	23.4

Table S5. The re-evaluated SHG coefficients with different band gaps. The bold values on the diagonal are the original ones.

$d_{22}(\times 10^{-9}$ esu)	E_g (Pb-Ti-O-F, 3.34 eV)	E_g (Pb-Nb-O, 3.67 eV)
d_{22} (Pb-Ti-O-F)	13.12	11.57
d_{22} (Pb-Nb-O)	4.39	4.31

Table S6. The re-evaluated SHG coefficients by replacing the band structure (E) or momentum matrix elements (M) of one compound with the other compound's. For example, the value corresponding to E(Pb-Ti-O-F) and M(Pb-Nb-O) means using the band structure from Pb₂TiOF(SeO₃)₂Cl and using the momentum matrix element from Pb₂NbO₂(SeO₃)₂Cl. The bold values on the diagonal are the original ones.

$d_{22}(\times 10^{-9}$ esu)	E(Pb-Ti-O-F)	E(Pb-Nb-O)
M(Pb-Ti-O-F)	13.12	7.30
M(Pb-Nb-O)	8.16	4.31

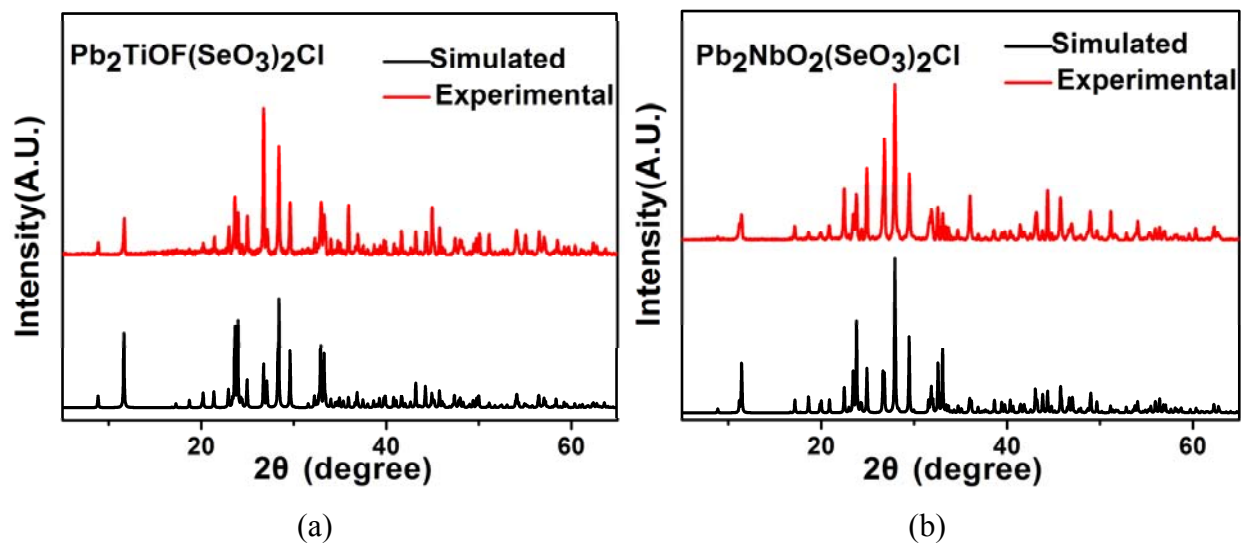


Figure S1. Simulated and experimental XRD powder patterns of $\text{Pb}_2\text{TiOF}(\text{SeO}_3)_2\text{Cl}$ (a) and $\text{Pb}_2\text{NbO}_2(\text{SeO}_3)_2\text{Cl}$ (b).

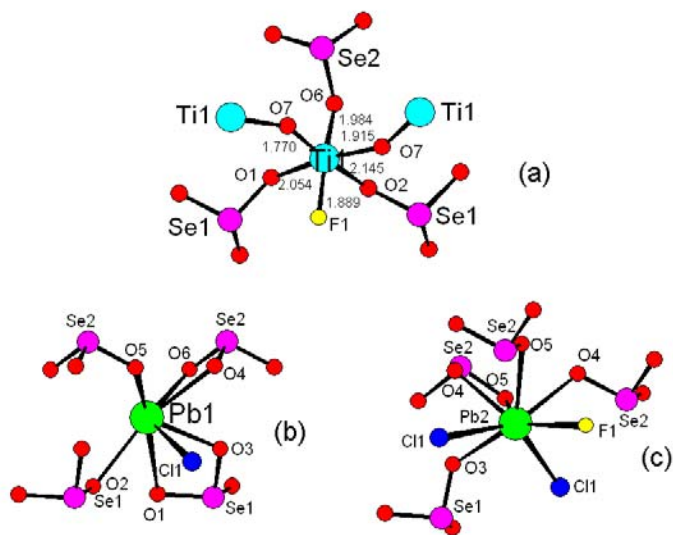
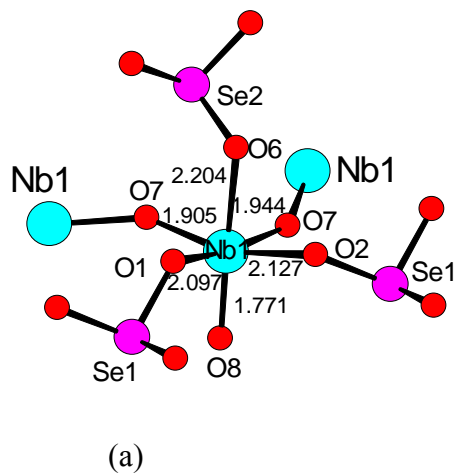


Figure S2. The coordination geometries around the Ti and Pb atoms in $\text{Pb}_2\text{TiOF}(\text{SeO}_3)_2\text{Cl}$.



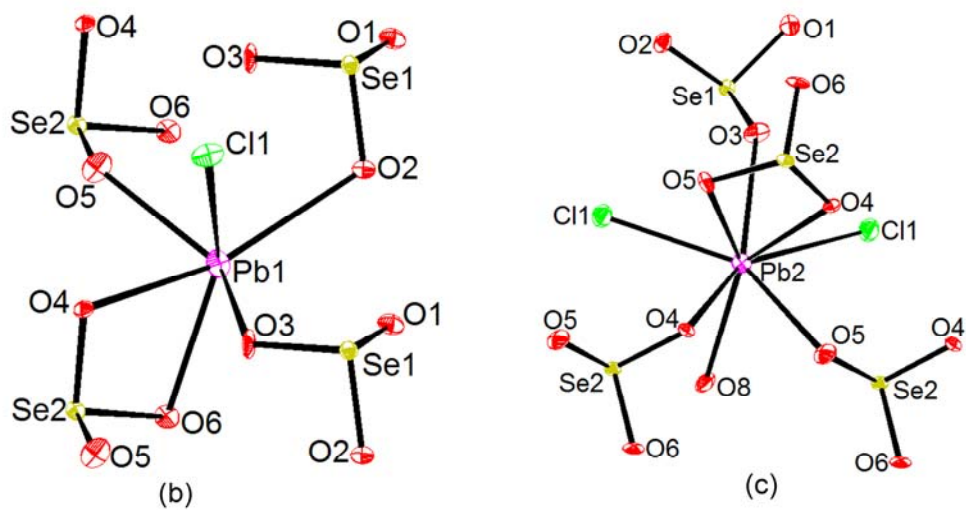


Figure S3. The coordination environments around the Nb atom (a), Pb(1) atom (b) and Pb(2) atom (c) in $\text{Pb}_2\text{NbO}_2(\text{SeO}_3)_2\text{Cl}$.

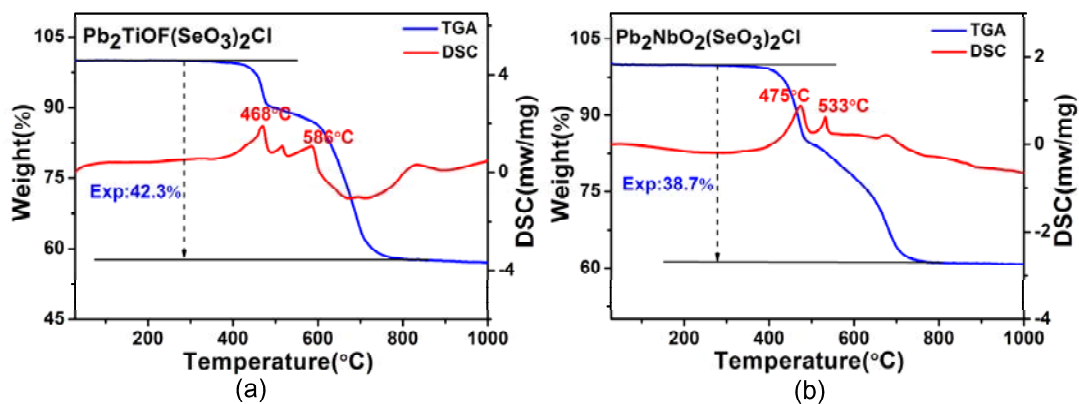


Figure S4. Thermogravimetric analysis (TGA) and Differential scanning calorimetry (DSC) curves of $\text{Pb}_2\text{TiOF}(\text{SeO}_3)_2\text{Cl}$ (a), and $\text{Pb}_2\text{NbO}_2(\text{SeO}_3)_2\text{Cl}$ (b).

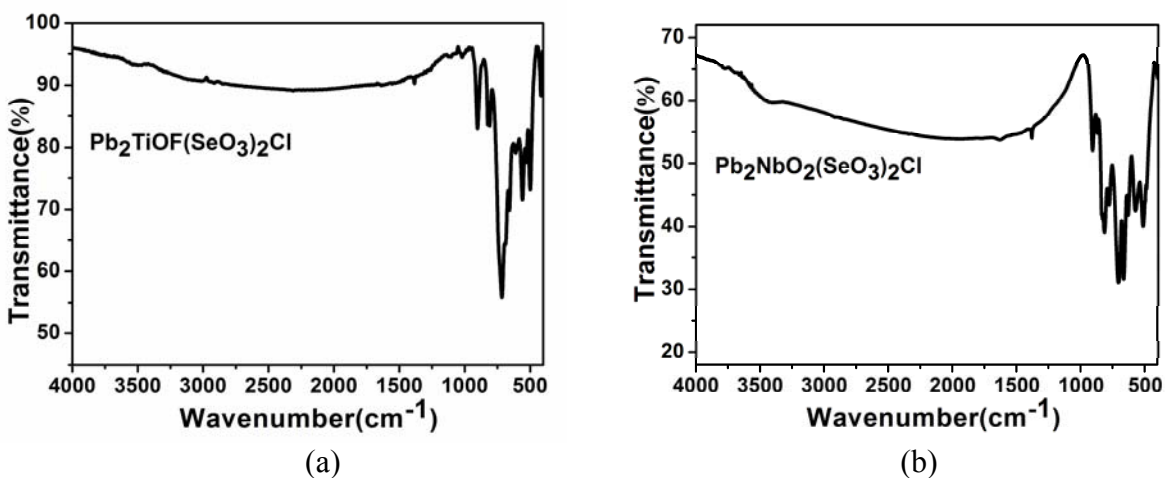


Figure S5. IR spectra of $\text{Pb}_2\text{TiOF}(\text{SeO}_3)_2\text{Cl}$ (a), and $\text{Pb}_2\text{NbO}_2(\text{SeO}_3)_2\text{Cl}$ (b).

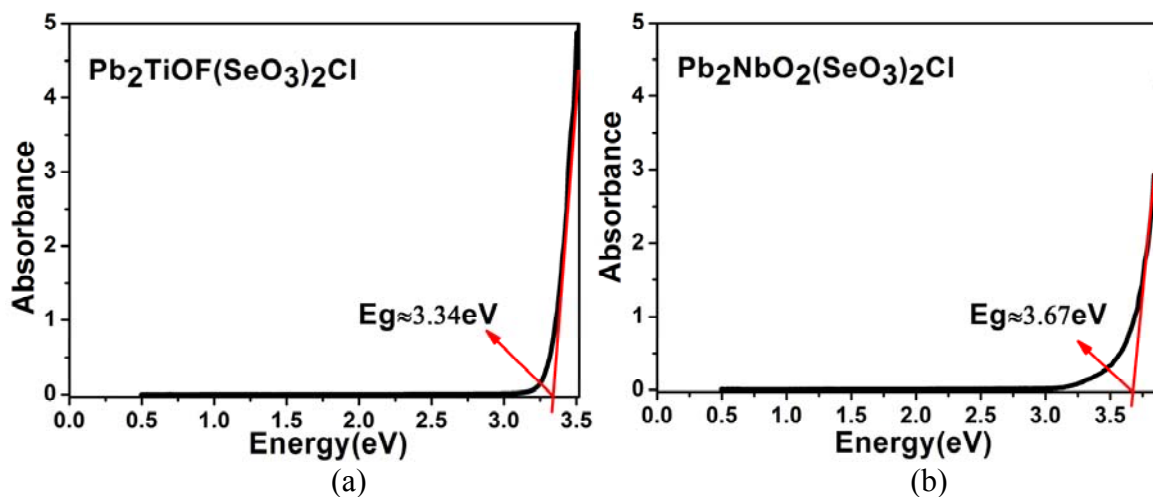


Figure S6. UV-Vis absorption spectra of $\text{Pb}_2\text{TiOF}(\text{SeO}_3)_2\text{Cl}$ (a) and $\text{Pb}_2\text{NbO}_2(\text{SeO}_3)_2\text{Cl}$ (b).

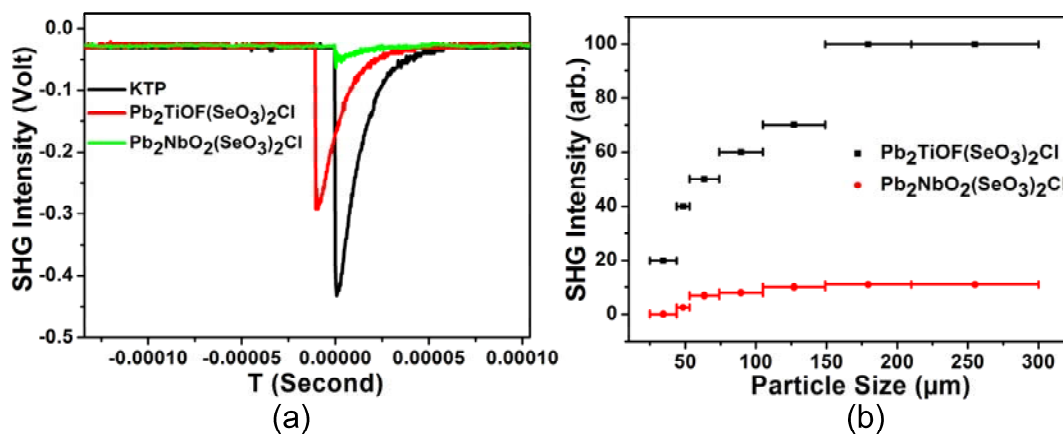


Figure S7. Oscilloscope traces of the SHG signals for the powders (149-210 μm) of KTP, $\text{Pb}_2\text{TiOF}(\text{SeO}_3)_2\text{Cl}$ and $\text{Pb}_2\text{NbO}_2(\text{SeO}_3)_2\text{Cl}$ (a), and phase-matching curve for $\text{Pb}_2\text{TiOF}(\text{SeO}_3)_2\text{Cl}$ and $\text{Pb}_2\text{NbO}_2(\text{SeO}_3)_2\text{Cl}$ (b) on a 2.05 μm Q-switched laser. The curve drawn is to guide the eye and not a fit to the data.

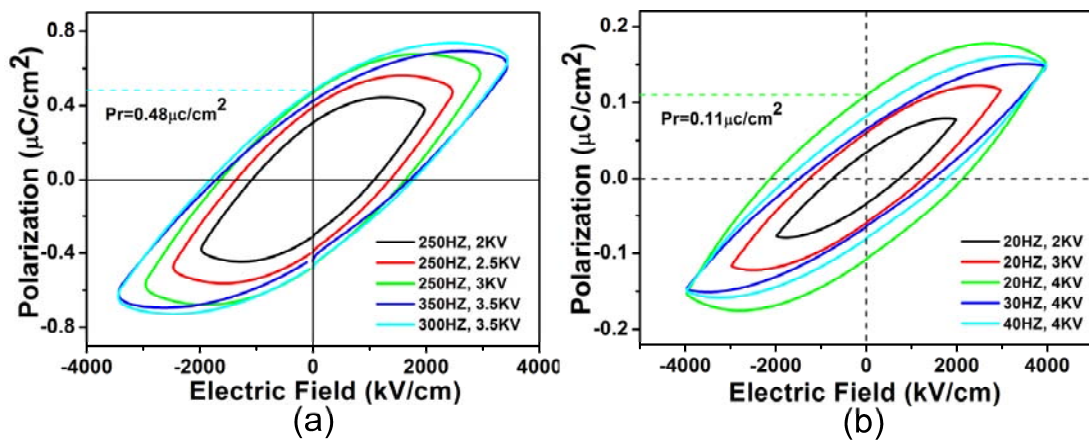


Figure S8. Polarization versus applied electric field for $\text{Pb}_2\text{TiOF}(\text{SeO}_3)_2\text{Cl}$ (a) and $\text{Pb}_2\text{NbO}_2(\text{SeO}_3)_2\text{Cl}$ (b).

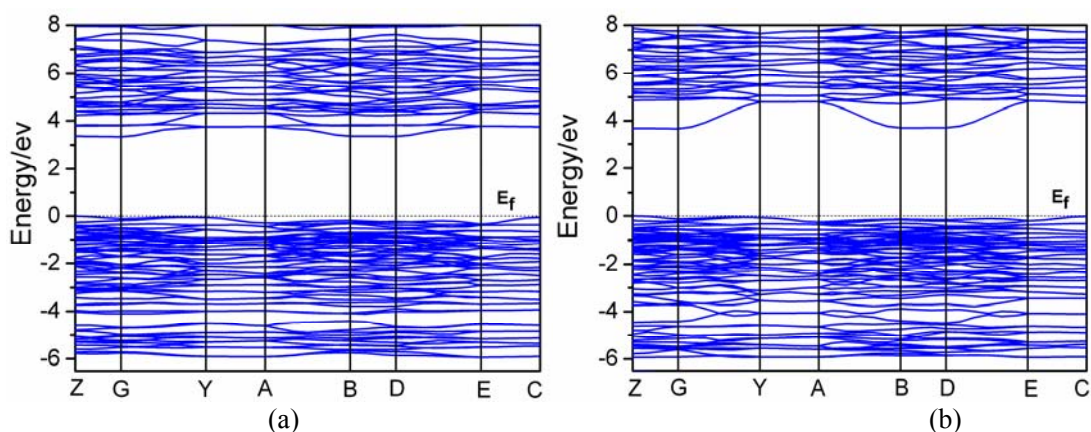


Figure S9. The scissor-added band structures of $\text{Pb}_2\text{TiOF}(\text{SeO}_3)_2\text{Cl}$ (a), and $\text{Pb}_2\text{NbO}_2(\text{SeO}_3)_2\text{Cl}$ (b).

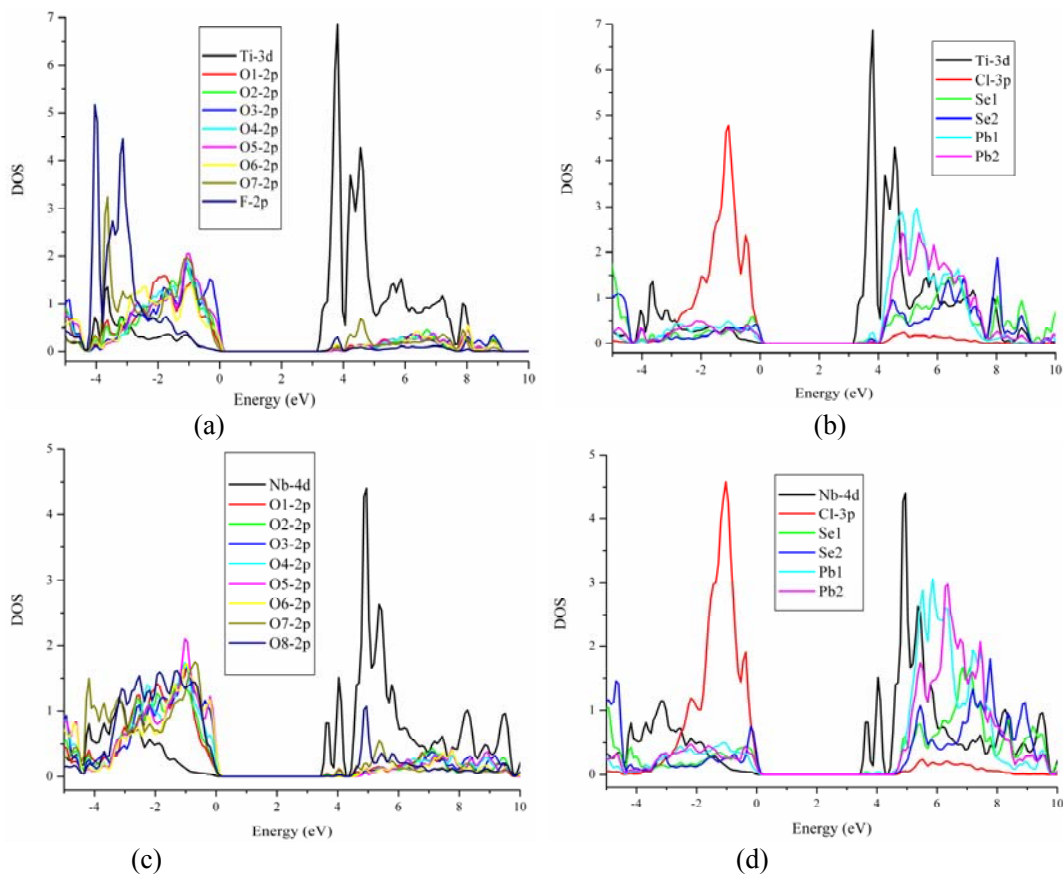


Figure S10. The partial density of states (PDOS) of $\text{Pb}_2\text{TiOF}(\text{SeO}_3)_2\text{Cl}$ (a-b) and $\text{Pb}_2\text{NbO}_2(\text{SeO}_3)_2\text{Cl}$ (c-d).

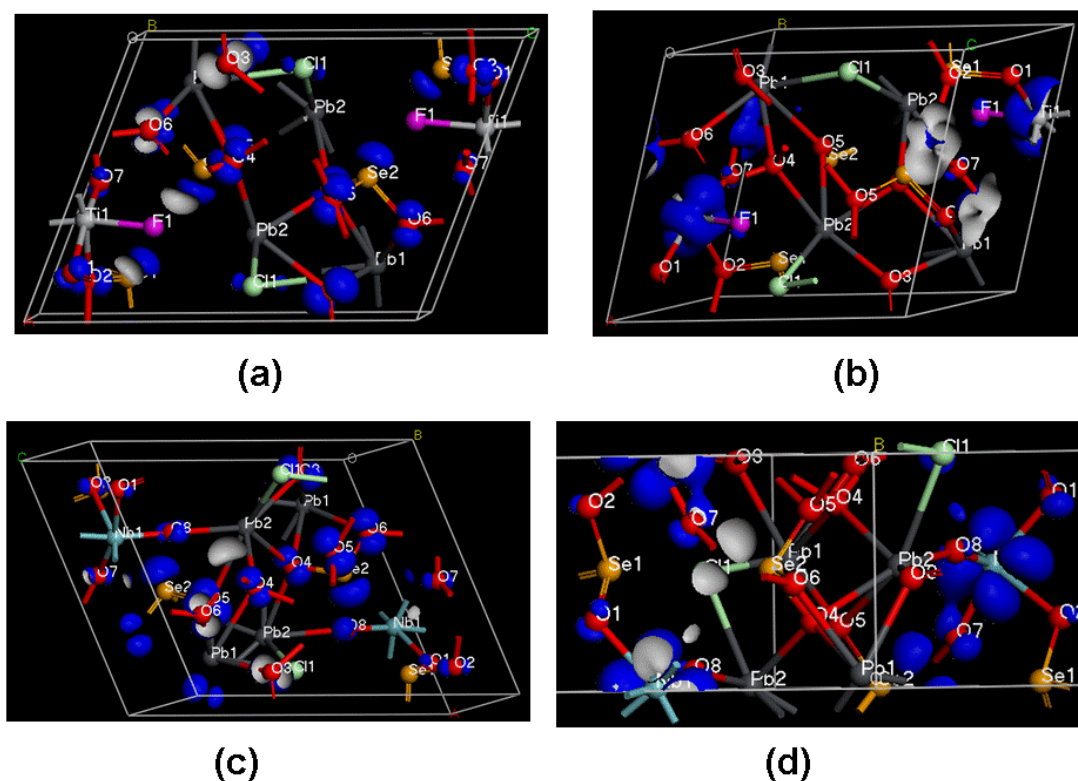


Figure S11. The highest occupied molecular orbital (HOMO) and the lowest unoccupied molecular orbital (LUMO) of $\text{Pb}_2\text{TiOF}(\text{SeO}_3)_2\text{Cl}$ (a: HOMO, b: LUMO) and $\text{Pb}_2\text{NbO}_2(\text{SeO}_3)_2\text{Cl}$ (c: HOMO, d: LUMO).

From the PDOS in Fig. S10, it is obvious that the valence band just below Fermi level is mostly contributed by O-2p, Cl-3p and small amount of Se-4p states, and the lowest conduction bands are mostly originated from Ti-3d (Nb-4d) and small amount of F-2p (little O-2p); and the Ti-F bond orbitals locate at the lower energy position than Ti-O and Nb-O bonds (in both VB and CB). Hence, $\text{Pb}_2\text{TiOF}(\text{SeO}_3)_2\text{Cl}$ has the smaller band gap. Meanwhile, we also see that the conduction bands of Nb-4d states are more dispersed than Ti-3d. In addition, orbital graphs can reveal the bonding properties more directly than the DOS graphs. From Fig. S11, we can see that the HOMO of two compounds are mainly contributed by non-bonding O-2p and Se-4p lone pairs;

the LUMO of $\text{Pb}_2\text{TiOF}(\text{SeO}_3)_2\text{Cl}$ reveals the relatively weak covalent interactions between Ti and F, while the LUMO of $\text{Pb}_2\text{NbO}_2(\text{SeO}_3)_2\text{Cl}$ exhibits the stronger covalent bonding between Nb and O.